Supplementary Information

Selective oxidation of glycerol over metal-free photocatalyst: Insights into the solvent effect on catalytic efficiency and products distribution

Pingbo Zhang[a, *], Chengguang Yue[a], Mingming Fan[a, *], Agus Haryono[b], Yan Leng[a],

Pingping Jiang[a]

[a] *The Key Laboratory of Synthetic and Biological Colloids, Ministry of Education, School of*

Chemical and Material Engineering, Jiangnan University, Wuxi 214122, P. R. China[1]

[b] *Research Center for Chemistry, Indonesian Institute of Sciences (LIPI), Kawasan Puspiptek,*

Serpong 15314, Indonesia

* Corresponding author. Tel.: +86 510 85917090; Tel.: +86 510 85917763.
E-mail addresses: pingbozhang@126.com, fanmm2000@126.com
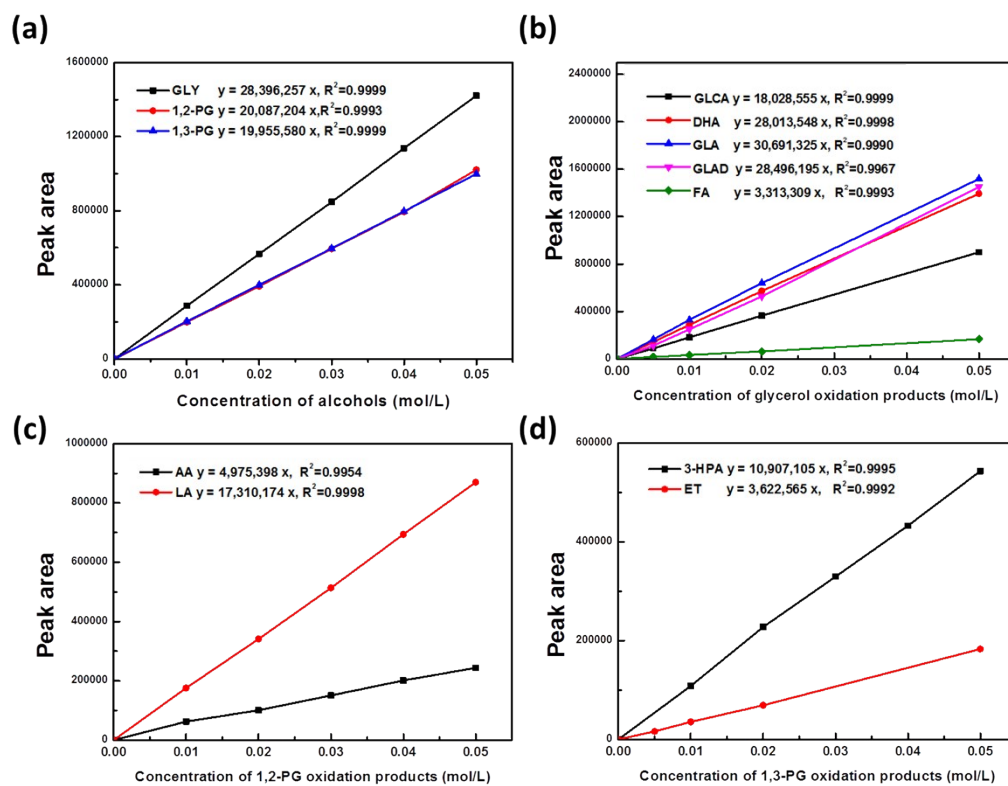
Section1. Standard curves

(a)

GLY   y = 28,396,257 x, R^2=0.9999
1,2-PG y = 20,087,204 x,R^2=0.9993
1,3-PG y = 19,955,580 x, R^2=0.9999

(b)

GLCA y = 18,028,555 x, R^2=0.9999
DHA   y = 28,013,548 x, R^2=0.9998
GLA   y = 30,691,325 x, R^2=0.9990
GLAD y = 28,496,195 x, R^2=0.9967
FA   y = 3,313,309 x, R^2=0.9993

(c)

AA y = 4,975,398 x, R^2=0.9954
LA y = 17,310,174 x, R^2=0.9998

(d)

3-HPA y = 10,907,105 x, R^2=0.9995
ET   y = 3,622,565 x, R^2=0.9992

Fig. S1 Standard curves of the detected substances

Section2. Details of LC-MS/MS

The LC-MS/MS was performed on an Ultra performance liquid chromatography-quadrupole tandem time-of-flight mass spectrometer. UPLC analysis was carried out with a Kinetex 2.6μ C18 100A (100×2.1 mm) column (Phenomenex). The mobile phase was a mixture of two solvents: A-water (0.1% FA) and B-acetonitrile. The optimized linear gradient system was as follows: 0 min, 95 % A; 0-1 min to 95% A; 1-10 min, to 1% A; 10-13 min, 1 % A; 13-13.1 min to 95% A; 13.1-16 min, 95% A. The autosampler was set to 4 °C. The injection volume was 5 μL, and the flow rate was 300 μl/min. The injection needle was washed after each injection with acetonitrile. The column oven was 40 °C. Mass spectrometry method: ion source temperature is

550℃, air curtain gas flow rate is 35pis, declustering voltage DP is 80(/-80) V, MS

mode collision energy is 10 eV, MS/MS mode collision voltage is 40±20 eV. The mass spectrum scan range is 100-1500 Da.

Table S1 LC-MS results of esters

Ester compound	Molecular formula	[M-H] measured molecular weight (Da)	[M-H] calculated molecular weight (Da)	Error （mDa）
2-hydroxy-3-((3-hydroxy-2-oxopropanoyl) oxy)propanoic acid (a)	$C_6H_8O_7$	191.0198	191.0192	0.6
2-((3-hydroxy-2-oxopropanoyl)oxy) acetic acid (b)	$C_5H_5O_6$	161.0089	161.0086	0.3
3-(formyloxy)-2-hydroxypropanoic acid (c)	$C_4H_6O_5$	133.0140	133.0137	0.3

(a)

Peak   MS   MSMS

(b)

Peak   MS   MSMS
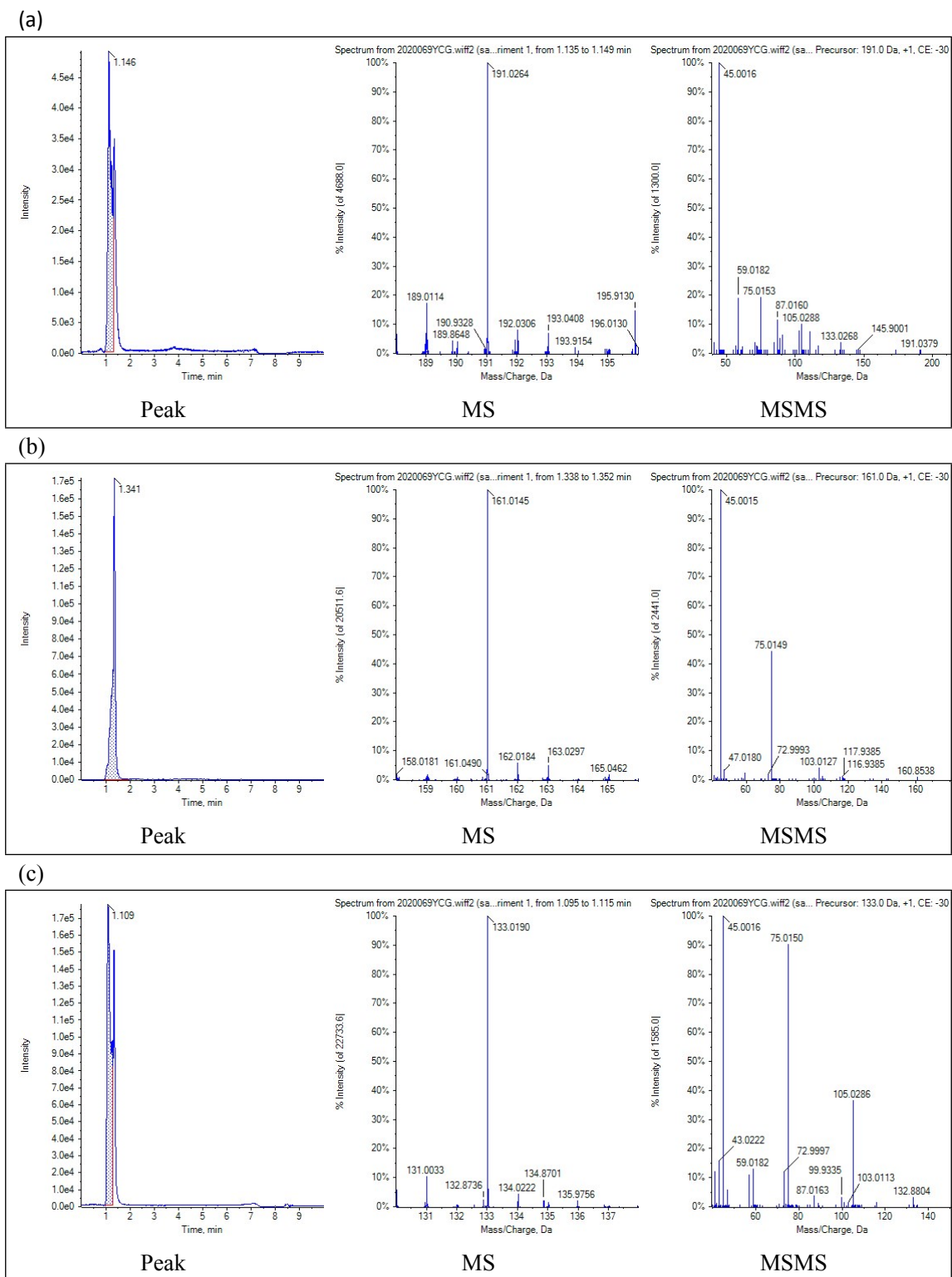
(c)

Peak   MS   MSMS
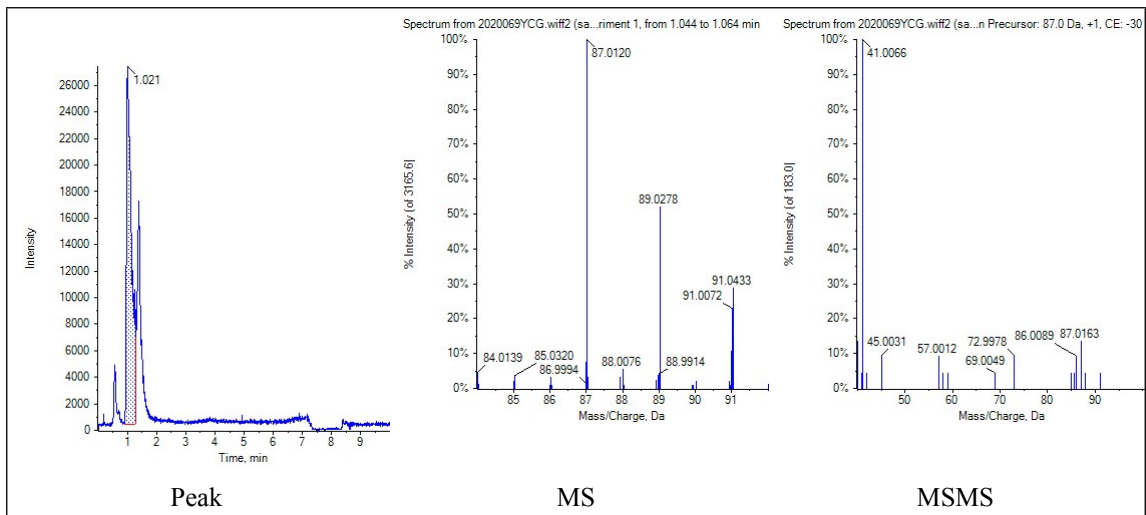
Fig. S2 LC-MS/MS spectra of esters

Fig. S3 LC-MS/MS spectra of HPAD

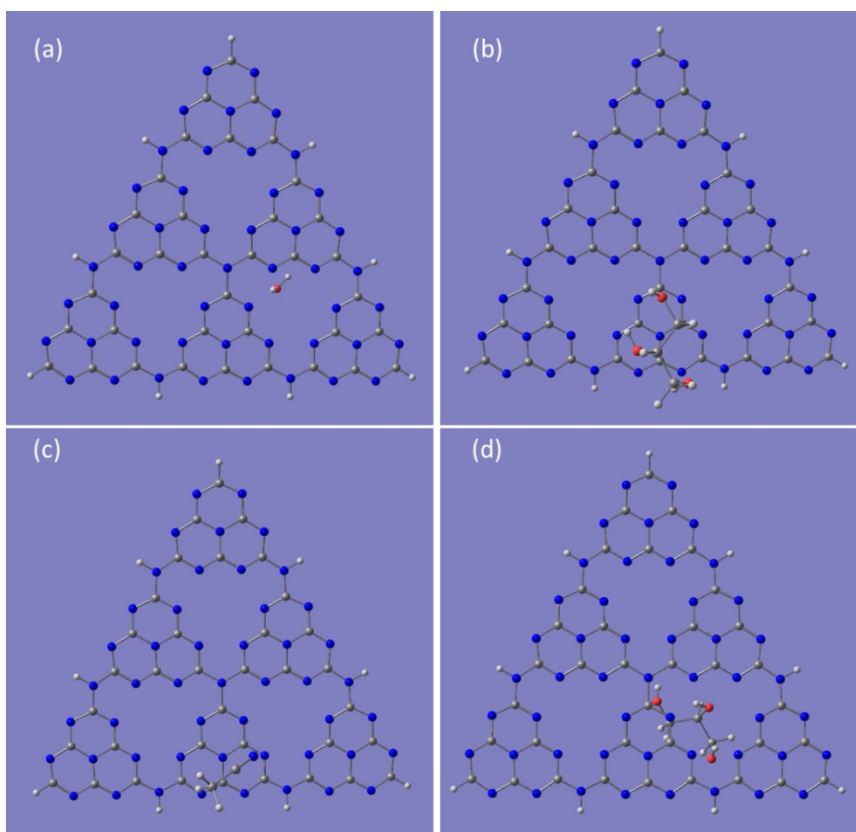# Section3. Optimum geometries

Fig. S4 Optimum geometries of H_2O (a) and glycerol (b) on g-C_3N_4 in water; CH_3CN (c) and glycerol (d) on g-C_3N_4 in acetonitrile

Section 4. H₂O₂ determination and glycerol adsorption
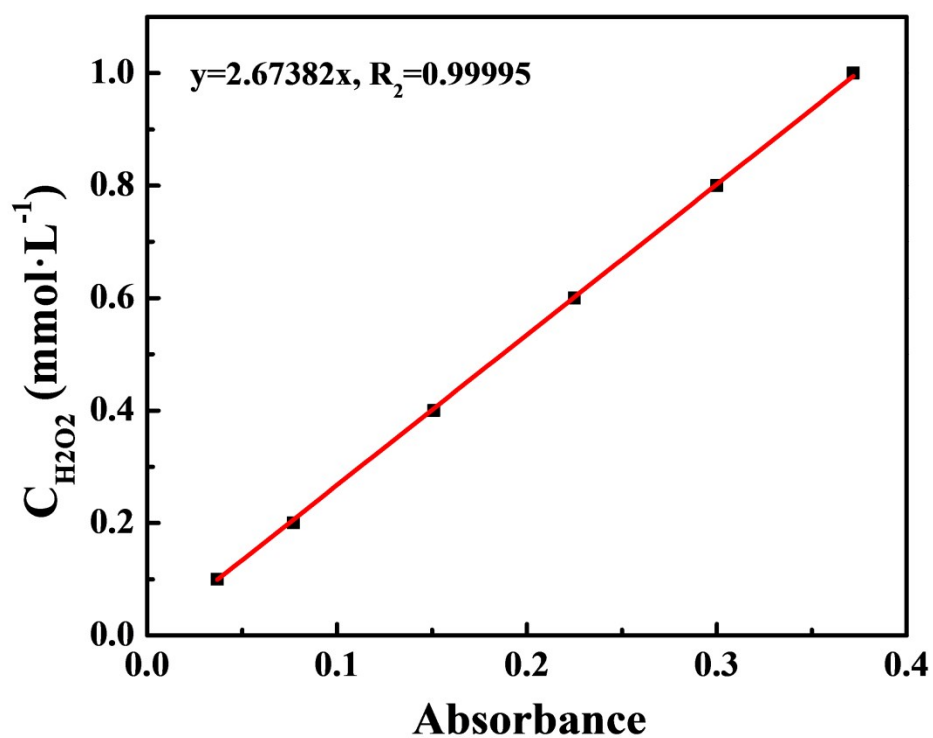

$y=2.67382x$, $R_2=0.99995$

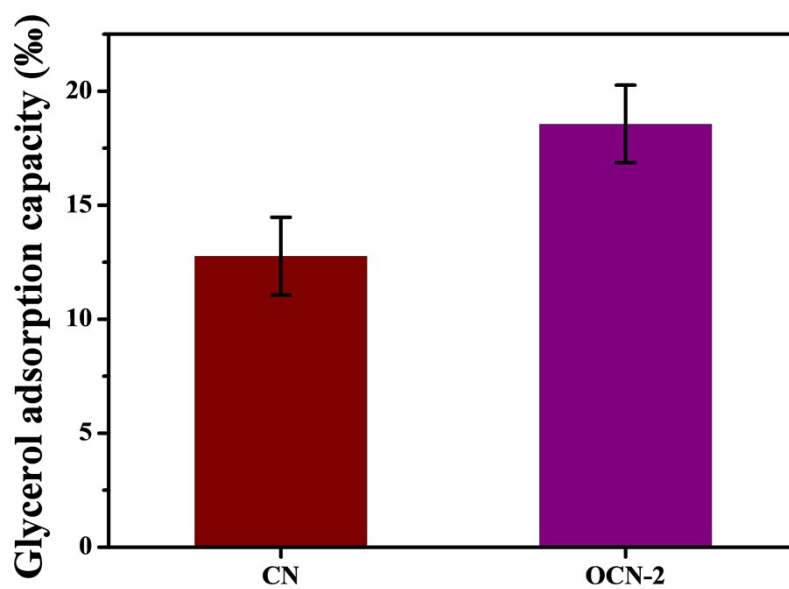**Fig. S5** Standard curve of absorbance and hydrogen peroxide concentration

Fig. S6 Adsorption of glycerol over CN and OCN-2 in acetonitrile

Section 5. Catalyst characterization methods and results

Methods： The morphological characterization of as-prepared samples was carried out using a field emission scanning electron microscope (Hitachi, S-4800). The specific surface area of catalysts was measured according to the Brunauer–Emmet–Teller (BET) method with N_2 adsorption–desorption on ASAP 2020 instrument (Micromeritics). X-ray diffraction (XRD) patterns were gotten via Bruker D8 Advance powder diffractometer using Cu K_α radiation source ($\lambda = 1.5406$ Å) at 40 kV and 40 mA from 10° to 50° with a scan rate of 4°/min. FT-IR spectra were recorded by infrared spectrometer (Thermo Fisher Scientific, Nicolet 6700). XPS spectra were recorded by a X-ray photoelectron spectrometer(Thermo Fisher Scientific, K-Alpha+) with Al Kα line as the excitation source and adventitious carbon (284.8 eV for binding energy) was used as reference to correct the binding energy of sample. Organic elemental analysis (OEA) was used to analyze the elemental content of the samples using elemental analyzer (Elementar, Vario EL cube). UV–vis diffuse reflectance spectra (DRS) were measured on a UV-3600 plus spectrophotometer (Shimadzu). The photoluminescence (PL) intensities were obtained on a FS5 fluorescence spectrophotometer (Edinburgh Instruments) with an excitation wavelength of 350 nm. Electron paramagnetic resonance (EPR) spectra were acquired using a Bruker A300 spectrometer.

Results： Fig. S7 shows the FESEM images of CN, CNN, OCN-2, and OCNN-2. As we can see, the CN (Fig. S7a) exhibits a bulk structure formed by layered structure. After the second calcination, CNN (Fig. S7b) shows a large flaky structure, this proves that thermal treatment can make the layered structure of CN thinner. The OCN-2 (Fig. S7c) shows a bulk structure similar to CN, while OCNN-2 (Fig. S7d) exhibits smaller flaky structure than that of CNN and the edges of OCNN-2 are curled which indicating its flaky structure is much thinner. Combining the results of the N_2 adsorption-desorption curves of the as-prepared catalysts given in Fig. S8, it can be seen that the specific surface area of CNN which was etched out by heat increases compared to CN, while OCNN-2 performs a larger specific surface area than CNN. This change should attribute to the effect of oxygen doping. We believe that the introduction of oxygen atoms leads to the deterioration of the stability of the catalyst framework. During thermal etching, more thermal corrosion points appeared at the oxygen doping points, which can cause the catalyst's structure partly decomposing to form the pore structure. Then the dense pores gradually became larger as the thermal etching progressing, and finally the large flakes of catalyst were divided into nanosheets with curved edges. It's believed that thinner lamellar structure and larger surface area are preferred for catalytic reactions since they can improve the transfer of charge carriers and increase the contact with the reactant molecules, which has been proved by the activity test of catalyst.[1] In addition, the results of XRD and FT-IR characterization (Fig. S9) showed that oxygen doping did not destroy the main

chemical structure of g-C$_3$N$_4$.

Organic elemental analysis (OEA) was applied to analyze the elemental content of CNN and OCNN-2, the result was shown in Table S2. The O content of OCNN-2 (2.0%) is higher than that of CNN (0.2%) and the N content of OCNN-2 (60.7%) is lower than that of CNN (62.5%), while the C and H contents of CNN and OCNN-2 are similar. It should be noticed that the change amount of nitrogen and oxygen content is basically the same between OCNN-2 and CNN. Therefore, we speculate that the oxygen element in OCNN-2 was doped in the form of partially replacing the nitrogen element in the g-C$_3$N$_4$ framework. To verify the specific bonding form of the doped oxygen atoms in the framework, we analyzed the elemental valence state in the OCNN-2 using XPS. As shown in the Fig. S10, the XPS spectra of OCNN-2 show new peaks at 287.7 eV for C 1s and 531.3 eV for O 1s, which correspond to the C=O group.[2-4] Thus, we infer that the doped oxygen atoms in OCNN-2 replaced the nitrogen atoms of the CN framework and formed the C=O groups. Considering O atom possesses one more valence electron than N atom, extra electrons can be produced when OCNN-2 was illuminated with the right wavelength of light, which may improve the catalytic efficiency of the catalyst.

The photoabsorption properties of the as-prepared catalysts were investigated by UV–vis diffuse reflectance spectroscopy. In Fig. S11a, the intrinsic absorption edge of OCN-2 and OCNN-2 show red shift relative to CN and CNN which indicating that the band gap of OCN-2 and OCNN-2 narrows and the light absorption capacity of the oxygen-doped catalysts has been improved in both the ultraviolet region and the visible region, which means the light harvesting performance of OCNN-2 is promoted by thermal treatment and O-doping. While stronger light absorption capacity means that the catalyst has better photocatalytic performance under the same light intensity conditions. The bandgaps (Eg) derived from the Tauc plots using the Kubelka–Munk function are 3.00, 3.00, 2.93 and 2.96 eV for CN, CNN, OCN-2 and OCNN-2, respectively. And it is noted that there are Urbach's tails with 2.40 and 2.45 eV bandgap for OCN-2 and OCNN-2, respectively (Fig. S12). Urbach's tail represents the localized midgap state (sub-bandgap) that allows that material to absorb lower energy photons than the actual optical bandgap.[5] The appearance of midgap can be ascribed to that the O-doping effect changed the band structures of OCN-2 and OCNN-2. To determine the positions of band edges of CNN and OCNN-2, their Mott–Schottky plots were analyzed (as shown in Fig. S13), the measured flat band potential (E_{FB}) of CNN and OCNN-2 are -0.79 and -0.86 eV (vs Ag/AgCl, pH=7), respectively. As an n-type semiconductor, the E_{FB} of g-C$_3$N$_4$ can be adopted to evaluate the conduction band (CB) value with appropriate correction value.[6, 7] Combine the values of CB and Eg, the valence band (VB) value of CNN and OCNN-2 are determined as 1.91 and 1.80 eV (vs Ag/AgCl, pH=7), respectively. The difference between the values is consistent with the results of XPS valence band spectra as shown in Fig. S14. It is believed that photo-generated holes are involved in the elimination of β-H in the photocatalytic oxidation of glycerol, and the valence band position of the photocatalyst determines the oxidation ability of the photo-generated holes.[8, 9] According to existing studies, 1.80 eV is an appropriate valence

band position, which makes the photo-generated holes generated in the valence band sufficient to achieve the elimination of β-H[10] and avoid the generation of hydroxyl radicals with strong oxidizing ability (E(•OH/H_2O) = 2.38 eV vs NHE, causing the peroxidation of products).[8, 11]

The steady-state photoluminescence (PL) also provides useful information as shown in Fig. S11b, the red shift of the PL emission peak from 462 to 485 nm is in agreement with the change of band gap. The intensity of PL emission peak in OCN is much higher than CN which indicated that OCN can product more electrons and hole under the same light intensity considering the O-doped catalysts have better light harvesting performance and O atom possesses one more valence electron than N atom. In addition, the much lower intensity of PL emission peak in CNN and OCNN-2 reflects the lower probability of the electron-hole recombination which attributes to the thinner flaky structure caused by thermal etching.[12]
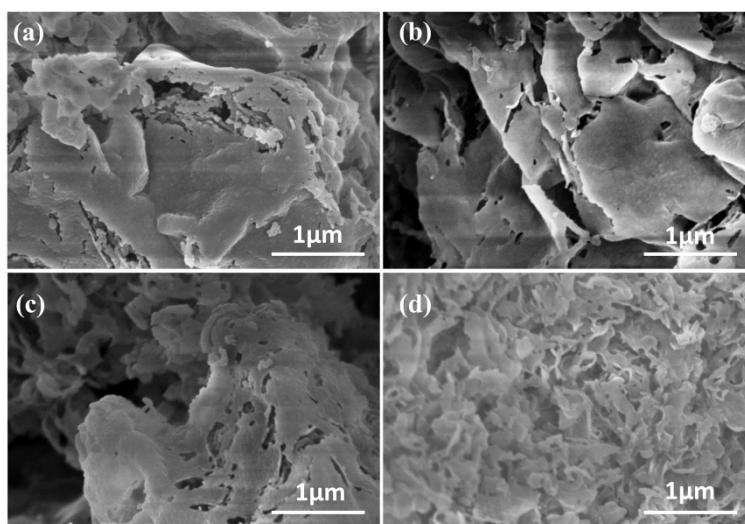

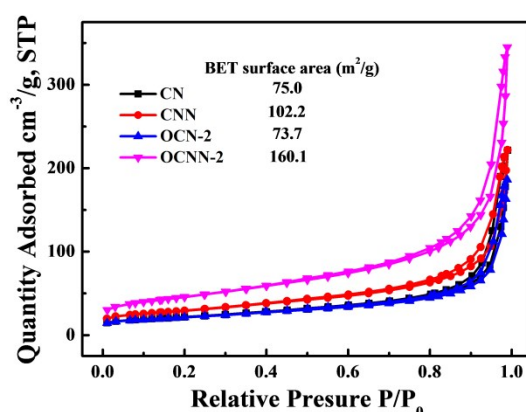**Fig. S7** FESEM images of (a) CN, (b) CNN, (c) OCN-2, (d) OCNN-2

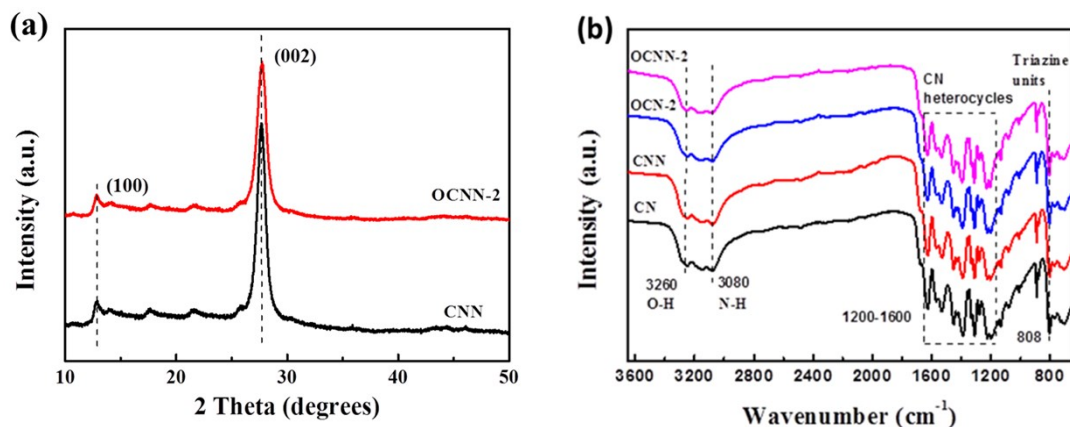**Fig. S8** N_2 adsorption-desorption isotherms of CN, CNN, OCN-2, OCNN-2

Fig. S9 (a) XRD patterns of CNN and OCNN-2; (b) FT-IR spectra of CN, CNN, OCN-2, OCNN-2

Table S2 Results of organic elemental analysis

Sample	C (Atomic %)	N (Atomic %)	H (Atomic %)	O (Atomic %)
CNN	35.5	62.5	1.9	0.2
OCNN-2	35.4	60.7	2.0	2.0

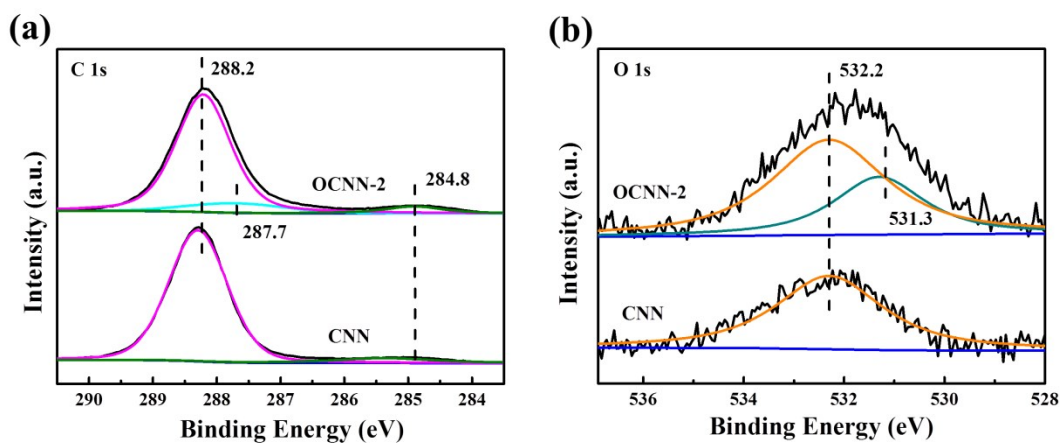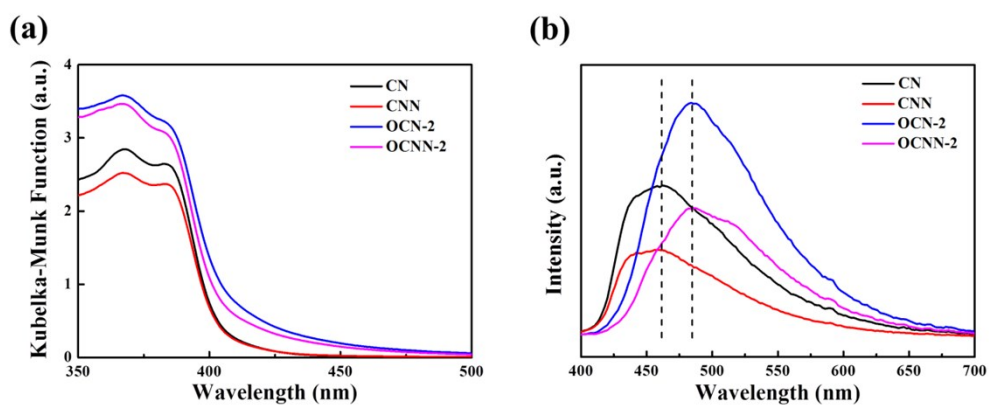**Fig. S10** XPS spectra of CNN and OCNN-2: (a) C 1s, (b) O 1s

Fig. S11 (a) UV−visible diffuse reflectance spectra and (b) Steady-state photoluminescence

spectra of CN, CNN, OCN-2, OCNN-2(the excitation wavelength was 350 nm)
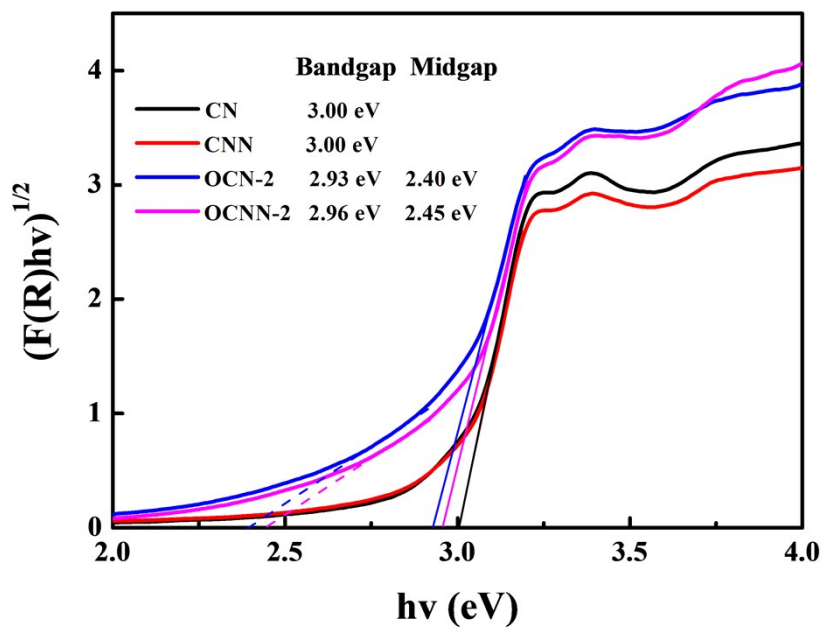

Fig. S12 Bandgap analysis through modification of the Kubelka−Munk function for the above samples, BaSO$_4$ was used as the reference
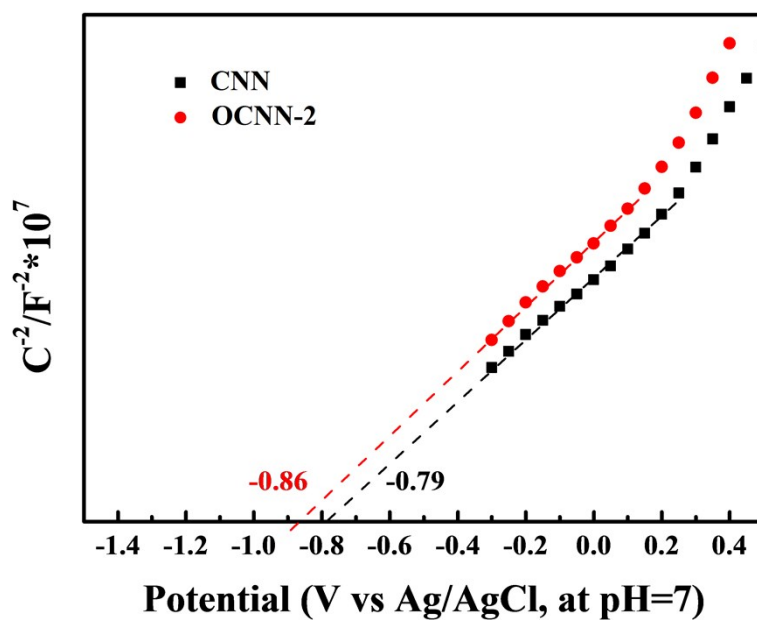

Fig. S13 Mott−Schottky flat band potential analysis for CNN and OCNN-2
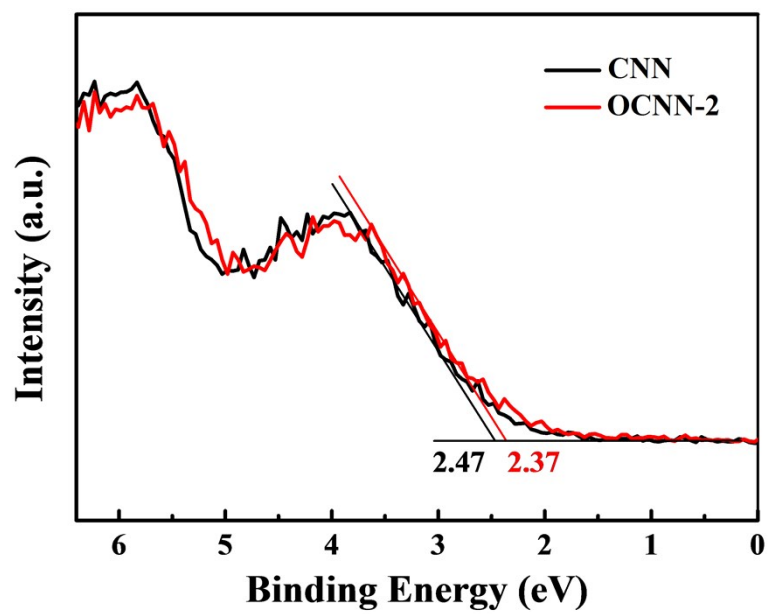
Fig. S14 XPS valence band spectra

Refrences

1. P. Niu, M. Qiao, Y. Li, L. Huang and T. Zhai, *Nano Energy*, 2018, **44**, 73-81.

2. H. Wang, S. Jiang, S. Chen, D. Li, X. Zhang, W. Shao, X. Sun, J. Xie, Z. Zhao, Q. Zhang, Y. Tian and Y. Xie, *Adv. Mater.*, 2016, **28**, 6940-6945.

3. W. Jiang, Q. Ruan, J. Xie, X. Chen, Y. Zhu and J. Tang, *Appl. Catal. B: Environ.*, 2018, **236**, 428-435.

4. F. Li, M. Han, Y. Jin, L. Zhang, T. Li, Y. Gao and C. Hu, *Appl. Catal. B: Environ.*, 2019, **256**.

5. C. H. Choi, L. Lin, S. Gim, S. Lee, H. Kim, X. Wang and W. Choi, *ACS Catal.*, 2018, **8**, 4241-4256.

6. W.-J. Chun, A. Ishikawa, H. Fujisawa, T. Takata, J. N. Kondo, M. Hara, M. Kawai, Y. Matsumoto and K. Domen, *J. Phys. Chem. B*, 2003, **107**, 1798-1803.

7. H. You, Z. Wu, L. Zhang, Y. Ying, Y. Liu, L. Fei, X. Chen, Y. Jia, Y. Wang, F. Wang, S. Ju, J. Qiao, C. H. Lam and H. Huang, *Angew. Chem. Int. Ed. Engl.*, 2019, **58**, 11779-11784.

8. Y. Zhang, N. Zhang, Z.-R. Tang and Y.-J. Xu, *Chem. Sci.*, 2013, **4**.

9. S. Zhao, Z. Dai, W. Guo, F. Chen, Y. Liu and R. Chen, *Appl. Catal. B: Environ.*, 2019, **244**, 206-214.

10. D. Liu, J. C. Liu, W. Cai, J. Ma, H. B. Yang, H. Xiao, J. Li, Y. Xiong, Y. Huang and B. Liu, *Nat. Commun.*, 2019, **10**, 1779.

11. Y. Nosaka and A. Y. Nosaka, *Chem. Rev.*, 2017, **117**, 11302-11336.

12. J. Q. Tian, Q. Liu, A. M. Asiri, K. A. Alamry and X. P. Sun, *Chemsuschem*, 2014, **7**, 2125-2130.